# Experimental investigation of turbulence-driven secondary motion over a streamwise external corner

By KHALID A. M. MOINUDDIN, P. N. JOUBERT
AND M. S. CHONG

Department of Mechanical Engineering, The University of Melbourne, Victoria 3010, Australia

Turbulence-driven secondary motion (known as secondary flow of Prandtl's second kind) is the result of the anisotropy of Reynolds stresses. It is associated with internal or external turbulent flow in the vicinity of streamwise corners. In the last six decades the flow along the streamwise internal corner has attracted the attention of many researchers, but it is only recently at the University of Melbourne that an experimental investigation on a flow over an external corner has been undertaken. Although the turbulence-driven secondary motions are generally much smaller than those resulting from skewing of the mean spanwise vorticity (known as secondary flow of Prandtl's first kind), they have a pronounced effect on peripheral wall shear stress distributions and heat transfer rates in the corner region. In the present study the details of turbulence-driven secondary motion over the external corner are explored experimentally and a counter-rotating helical streamwise vortex pair symmetrically placed around the corner bisector is found. As expected, all mean velocity and Reynolds stress profiles on both surfaces at the same spanwise distance from the corner agree quite well, having nominal deviation. The secondary flow is observed to be directed away from the corner bisector and then flow back towards the wall. It is also revealed that far from the corner, the flow develops as a nominal two-dimensional flat-plate boundary-layer flow.

## 1. Introduction

The study of the three-dimensional turbulent boundary layer developing over a streamwise external corner (chine) has considerable significance in various engineering applications. This flow includes many of the phenomena seen in turbulent flows encountered in practice such as on ship hulls, on some aircraft bodies and on long transport vehicles like trains, trucks and buses. A chine is formed at the longitudinal intersection of two flat surfaces. Flow past the longitudinal edge of a finite flat plate aligned with the streamwise direction has been studied by Elder (1960) and Davies & Young (1963). With the addition of a second flat plate held normal to the first, but parallel to the free stream, a streamwise corner region is formed (see figure 1).

Secondary flow is a generic term used to denote the mean cross-flow field characterized by the velocity components $V$ and $W$ that lie in the $(s, n)$-plane (figure 1$b$) which is normal to the main flow direction, $x$. By taking the derivatives of $V$ and $W$, longitudinal vorticity can be found. The streamwise vorticity transport
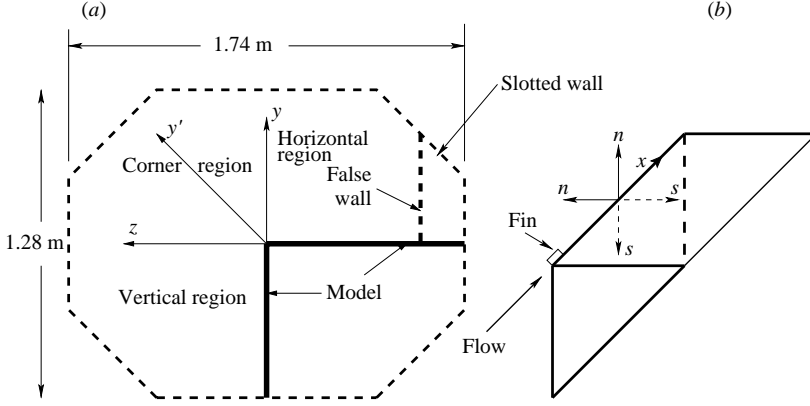
FIGURE 1. Schematic diagram of (a) tunnel cross-section and (b) model, presented looking downstream.

equation is

$$U\frac{\partial \Omega_x}{\partial x} + V\frac{\partial \Omega_x}{\partial y} + W\frac{\partial \Omega_x}{\partial z} = \nu\left(\frac{\partial^2 \Omega_x}{\partial x^2} + \frac{\partial^2 \Omega_x}{\partial y^2} + \frac{\partial^2 \Omega_x}{\partial z^2}\right)$$
$$\underbrace{\hphantom{U\frac{\partial \Omega_x}{\partial x} + V\frac{\partial \Omega_x}{\partial y} + W\frac{\partial \Omega_x}{\partial z}}}_{A1} \qquad \underbrace{\hphantom{\nu\left(\frac{\partial^2 \Omega_x}{\partial x^2} + \frac{\partial^2 \Omega_x}{\partial y^2} + \frac{\partial^2 \Omega_x}{\partial z^2}\right)}}_{A2}$$

$$+ \underbrace{\Omega_x\frac{\partial U}{\partial x} + \Omega_y\frac{\partial U}{\partial y} + \Omega_z\frac{\partial U}{\partial z}}_{A3} + \underbrace{\left(\frac{\partial^2}{\partial y^2} - \frac{\partial^2}{\partial z^2}\right)(\overline{-v'w'})}_{A4} + \underbrace{\frac{\partial^2}{\partial y\partial z}(\overline{v'^2} - \overline{w'^2})}_{A5}, \quad (1.1)$$

where

$$\Omega_x = \frac{\partial W}{\partial y} - \frac{\partial V}{\partial z}. \tag{1.2}$$

Terms (A1) on the left-hand side of the equation represent the convection of streamwise vorticity by the mean motion. The first term (A2) on the right-hand side expresses the damping by viscosity, the second group of terms (A3) demonstrate the vortex stretching and tilting by the mean velocity gradients and the next two terms, (A4) and (A5), represent the contribution of Reynolds secondary shear stresses and normal stresses respectively, to the production or destruction of streamwise vorticity.

There are two main kinds of secondary flows: skew-induced (Prandtl's first kind) and stress-induced (Prandtl's second kind). The terms in (A3) of equation (1.1) are responsible for generating the first kind, whereas the second kind is attributed to (A4) and (A5). Prandtl (1926) was the first to recognize that turbulent flow in ducts of non-circular cross-section belongs to the second kind of secondary flows. The secondary flow velocities induced by turbulence are generally smaller than those resulting from skewing of a pre-existing shear layer. The main evidence of a secondary flow of the second kind is given by the isotachs (isovelocity contours), which show a distortion near the corners of the duct (Gessner & Jones 1965). Early studies show that the secondary flow along the bisector of the internal corner is directed towards the corner in turbulent flow as shown in figure 2. Zamir & Young (1970) reported the opposite distortion in laminar flow to that of turbulent flow and indicated that the phenomenon might result from an instability of these flows which takes the form of streamwise vortices before proper transition. However, as the second kind of secondary flow is
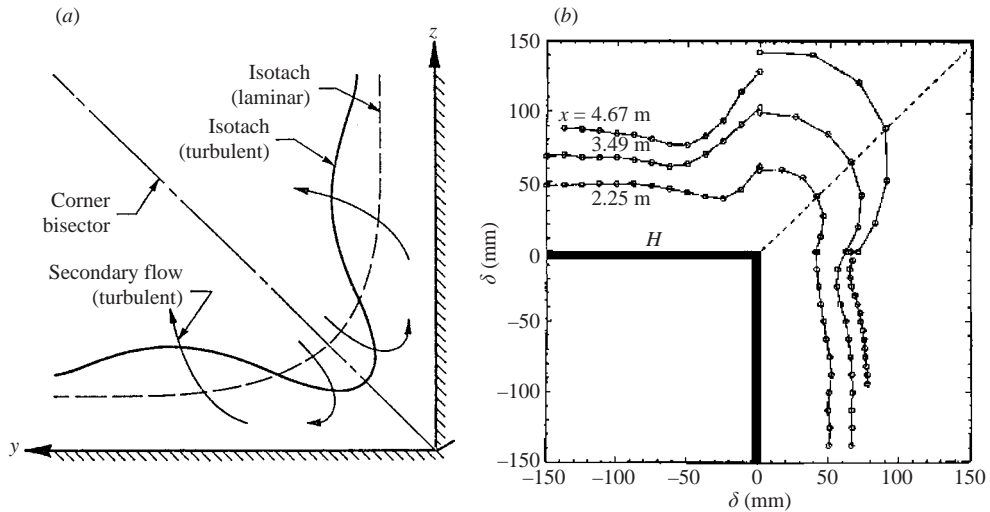
FIGURE 2. (*a*) A sketch of the flow structure in the internal corner region of a straight duct (from Gessner 1973). (*b*) Boundary layer thickness distribution of Panchapakesan & Joubert (1998) for an external corner (presented looking upstream).

generated by the anisotropy of Reynolds stresses, it should not have any counterpart in laminar flow (Bradshaw 1987).

Since the experimental study of Nikuradse (1930), a number of similar studies of the boundary layer in the internal corner region have been reported. A comprehensive literature survey of experimental and numerical studies is given in Moinuddin *et al.* (2003). Xu & Pollard (2001) carried out large-eddy simulations (LES) of a co-axial square duct which contains both concave (internal) and convex (external) corners. The results show strong interaction between the secondary flows developed on both the internal and external corners. They found a chain of counter-rotating vortex pairs symmetrically placed around the bisectors of both concave and convex orthogonal corners. At the University of Melbourne a unique series of experimental investigations on the external corner have been made by Panchapakesan & Joubert (1998, 1999), Moinuddin *et al.* (2001, 2003) and Moinuddin, Joubert & Chong (2002*b*). Their measurements showed, in qualitative terms, consistency with the general behaviour reported by Elder (1960) and Xu & Pollard (2001). These measurements also revealed, as one moves towards the corner from the two-dimensional region, first thinning of the boundary layer followed by thickening due to the secondary flow. The same initial thinning and subsequent thickening was also observed by Elder (1960) and Xu & Pollard (2001). Xu & Pollard (2001) revealed that for the external corner the secondary flow is driven away from the corner along the bisector and returns back towards the wall farther from the corner. Moinuddin *et al.* (2003) presented detailed mean flow measurements. Their measurements exhibit symmetry about the corner bisector in terms of reduced mean flow parameters with nominal deviation depending on spanwise and normal distance from the corner. Moinuddin *et al.* (2001, 2002*a*) have established the symmetry of this flow based upon mean flow measurements. They achieved a quasi-symmetric flow all along the model, with the introduction of some changes to the test model geometry. In this paper detailed turbulence measurements are presented with only the salient features of mean flow measurements included.

## 2. Experimental apparatus and techniques

The experiment was carried out in a large closed-circuit wind tunnel. The test section of the tunnel has an octagonal cross-section with major dimensions of 1.28 m by 1.74 m as shown in figure 1. The 6.54 m long test section is constructed from aluminium slats with narrow gaps between them. The blockage effect of the models, used in the test section, is minimized by this construction. The chine model, with some essential changes, is the same as that used and described by Panchapakesan & Joubert (1998).

In the previous investigation two plane surfaces, constructed from varnished medium-density fibre boards, of half the test section width and running the entire length of the test section, made up the chine. In the present model, 80 cm long flaps set at 10° to the main flow direction were attached at the downstream end of the model to prevent the development of any favourable pressure gradient and also to minimize the interaction between flow over and beneath the test model surface. The model surface was polished meticulously to a mirror-like finish. Aluminium aerofoils of a symmetric section were attached to the leading edges to avoid flow separation. As the initial measurements at an early station at $x = 1.07$ m exhibited asymmetry, which was attributed to the mismatch of the airfoils joint, a small fin (10 mm wide and 100 mm long) was placed at the top of this joint at an angle of 45° (for details see Moinuddin et al. 2002a). As described in Moinuddin et al. (2001) a false sidewall was also placed on the horizontal surface to ensure flow symmetry along the model.

Different tripping devices were used on the horizontal and vertical surfaces to ensure flow symmetry about the corner bisector. The trip wire on the vertical surface was fixed to the boards at about 180 mm from where the aluminium airfoil and the chine boards met. On the horizontal surface 100 mm wide sandpaper (40 grits) was placed and its trailing edge was aligned with a trip wire on the vertical surface. This is taken as the reference for axial distance measurements. For transverse and normal distances the corner and flat-plate surfaces are considered respectively as the reference. The flow regime is divided into three regions (horizontal, corner and vertical) as shown in figure 1(a). $x$ is the distance in the streamwise direction for all cases. Spanwise and normal directions are denoted by $s$ and $n$ respectively for the horizontal and vertical region as shown in figure 1(b). For the corner region $z$, $y$ and $y'$ represent spanwise, normal and corner bisector directions respectively (see figure 1a).

The flow was investigated at $6.8 \times 10^5$ unit Reynolds number corresponding to a nominal free-stream velocity of $10.5 \, \mathrm{m \, s^{-1}}$. A Pitot tube of 0.7 mm diameter was used for mean flow measurements and was calibrated against the NPL Prandtl tube. The Macmillan correction was applied to the readings. Similarly, a separate static pressure probe was calibrated against an NPL static tube for measuring coefficient of pressure ($C_p$) distribution. A Gould Datametric electronic manometer was used to record total pressure. For recording instantaneous temperature a thermocouple was used. A separate electronic manometer was used in the laboratory to record atmospheric pressure. All the output voltage signals were integrated using a Pentium 3 computer interfacing with a MSBX 028 simultaneous sampling board and DAP 4000a data acquisition hardware. The first measuring position was found by first traversing the Pitot tube towards the wall until it touched the wall. The Pitot tube was then traversed away from the wall in 0.05 mm increments until there was a noticeable change in the velocity measured. The first measurement point was then taken as the last measurement recorded before the change. In the current paper friction velocity ($U_\tau$) has been calculated from a Clauser chart. For scaling mean velocity components

| Station (m) | Measuring stations, $s$ (mm) | Profiles collapse (mm) | $Re_{\theta_{2D}}$ | $\delta_{2D}$ (mm) |
|---|---|---|---|---|
| $x = 0.540$ | 5, 10, 15, 20, 25, 30, 40, 50, 120 | $s > 15$ | 1850 | 22.584 |
| $x = 1.070$ | 5, 10, 15, 25, 30, 40, 50, 75 | $s > 10$ | 2600 | 31.865 |
| $x = 2.170$ | 5, 10, 15, 25, 30, 50, 75, 100 | $s > 25$ | 3750 | 45.996 |
| $x = 3.385$ | 5, 10, 15, 30, 50, 75, 100, 125 | $s > 30$ | 4975 | 59.857 |
| $x = 4.565$ | 5, 15, 30, 50, 75, 100, 125, 150 | $s > 50$ | 5700 | 72.720 |
| $x = 5.010$ | 5, 15, 30, 50, 75, 100, 125, 150 | $s > 30$ | 6075 | 78.995 |

TABLE 1. Table for mean flow velocity profiles.

and Reynolds stresses data, Xu & Pollard (2001) used the averaged $U_\tau$ value, whereas in the present study the local $U_\tau$ values are deemed to be more appropriate and therefore were used.

Constant-temperature hot-wire anemometry was used in all turbulence and secondary flow components measurements. Details of the electronic circuit and dynamic calibration procedure are close to those given in Perry (1982) and Kelso (1991). Dantec 55P05 single and 22P51 cross-hot-wire probes were used and the sensors were made using platinum Wollaston wire and were 5 µm in diameter and 1 mm in length. The distance measurement of the probe from the wall needs to be made as accurately as possible. From the mean velocity profile local skin friction coefficient ($C_f$) has been derived and its value is put in the Reichardt formula. The first measuring position was found by first measuring the local free-stream velocity with hot-wire and then traversing down the probe very close to the wall when the local velocity was measured. The exact wall distance was calculated based on the Reichardt formula using local free-stream velocity ($U_{hw}$), kinematic viscosity ($\nu$), $C_f$ and the local free-stream velocity from Pitot tube measurements ($U_{Pitot}$). The probe was further traversed towards the wall until the probe was less than 0.4 mm from the wall for a single wire and 3.2 mm for the cross-wire. As the first measurements nodes off the wall were at $n^+ (= nU_\tau/\nu) > 8$, no thermal compensation was used to account for near-wall influence. Durst & Zanoun (2002) showed that no correction for hot-wire measurements in the near-wall region is needed for $n^+ > 3.5$.

## 3. Preliminary investigations

### 3.1. $C_p$ distribution

Zero pressure gradient (ZPG) was maintained in the tunnel test section with the chine model inside the test section as shown in figure 1($a$). The streamwise $C_p$ distribution measured, along a line at 240 mm above and 340 mm away from the corner (in the corner region of figure 1$a$), was presented in figure 4 of Moinuddin *et al.* (2003). The result shows that in the current study, over the length of the plate there is only a very small reduction in the mean $C_p$ values and the local variation is quite small.

### 3.2. Pitot static tube measurements

The mean streamwise flow velocity profiles were measured with a Pitot static tube at six streamwise stations, i.e. at $x = 0.54$ m, 1.07 m, 2.17 m, 3.385 m, 4.565 m and 5.01 m and the detailed mean flow data have been presented in Moinuddin *et al.* (2003). A summary of the measurements is tabulated in table 1. It was noticed that on moving sufficiently away from the corner the boundary layer develops as a nominal two-dimensional flat-plate boundary layer. In table 1, $Re_{\theta 2D}$ and $\delta_{2D}$ are the Reynolds
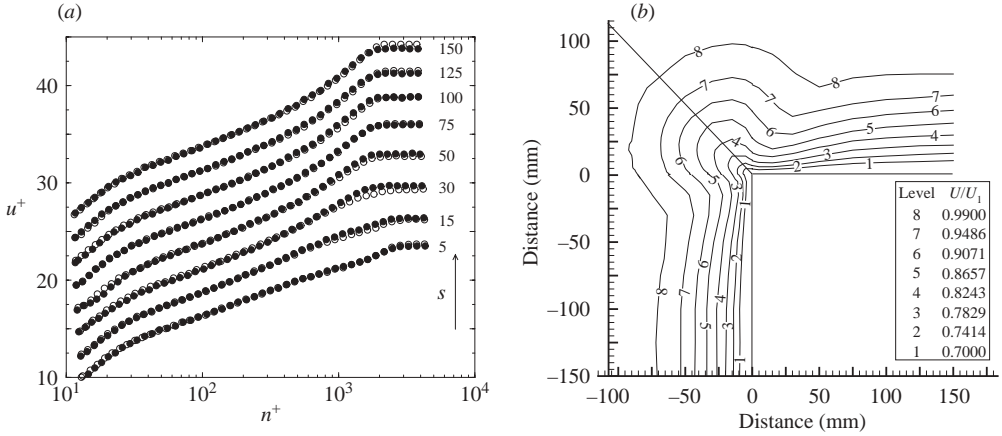
FIGURE 3. (a) Velocity profiles at different spanwise stations at $x = 4.565$ m. Profiles are shifted 2.5 units upwards from previous ones, except for the first profile at $s = 5$ mm. Open circles denote horizontal and filled circles vertical. (b) Isovelocity contours. Both figures are after Moinuddin *et al.* (2003).

number based on momentum thickness and the boundary layer thickness (where $U = 0.99 \, U_1$) in the two-dimensional region.

Isostreamwise velocity contours showed distortion near the corners with initial thinning of the boundary layer towards the corner away from the two-dimensional region and a subsequent thickening due to the secondary flow (see figure 3). This is an indication of the presence of secondary flow and the need for the measurements of mean spanwise and normal flow velocity profiles to obtain further insight into the secondary flow.

## 4. Three-dimensional mean flow field

Based on this preliminary study, mean spanwise and normal flow velocity profiles as well as Reynold stress profiles at three streamwise stations, i.e. at $x = 0.54$ m, 1.07 m and 4.565 m were taken with cross-wires. At $x = 4.565$ m, mean streamwise flow velocity profiles were also measured with a single hot-wire and an excellent agreement between Pitot tube and normal wire measurements was observed (see Moinuddin *et al.* 2002b). The streamwise mean flow velocity profiles on both surfaces, at the same streamwise and spanwise stations, were plotted together in Moinuddin *et al.* (2003). The results showed quasi-symmetry along the model with a maximum 10% deviation in reduced mean flow parameters. The profiles almost completely collapse at some distance from the corner (tabulated in column 3 of table 1). As the boundary layer is quite thick at $x = 4.565$ m, (where $Re_\theta = 5700$ in the nominal two-dimensional region) the measurements are expected to have much better spatial resolution. Therefore, primary flow velocity data at this downstream station are presented in the present paper.

### 4.1. *Primary velocity*

The streamwise mean flow velocity profiles on both surfaces are plotted in figure 3(a). In the figure, $s$ is the spanwise distance from the corner, $u^+$ is the non-dimensional mean streamwise local velocity normalized by $U_\tau$ and $n^+$ $(= nU_\tau/\nu)$ is the non-dimensional normal distance from the flat-plate surface. The figure shows symmetrical
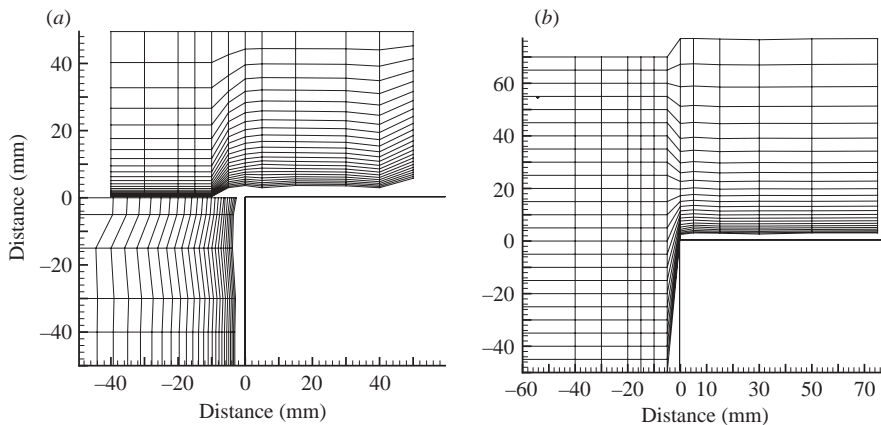
FIGURE 4. Cross-wire measurement grid (*a*) at $x = 0.54$ m and (*b*) at $x = 1.07$ m.

development of boundary layer and velocity profiles. Reduced mean flow parameters on both the surfaces show a nominal 5% deviation (see Moinuddin *et al.* 2001). The profiles almost completely collapse beyond $s = 100$ mm and a nominal two-dimensional flat-plate boundary layer develops further away from the corner. Slight differences in skin friction on the two surfaces again caused small differences in the outer layer in some profiles in the two-dimensional region. This difference may also be due to the influence of the growing corner vortices between the tunnel bottom wall and vertical surface and between the horizontal surface and false sidewall.

In the corner region (see figure 1*a*), measurements were taken at $z = 5, 15, 30, 50, 70, 90, 110$ mm. Based on these Pitot static tube measurements, isostreamwise velocity contours are drawn using a plotting and visualization software 'Tecplot' and they are plotted in figure 3(*b*). In this software, a number of data points are generated by linearly interpolating input data in both horizontal and vertical directions and then contours are drawn by straight line connection of these data points. In figure 3(*b*), $U_1$ represents local free-stream velocity and this symbol is used throughout this paper.

The boundary layer thickness, $\delta$, grows almost equally about the plane of symmetry, with only a small variation at the outer edge of the contours near the corner of the chine. This indicates that the outer region is strongly influenced by edge (of chine) turbulence. The initial thinning and then thickening of the boundary layer from the two-dimensional region towards the corner is quite evident. This phenomenon is strongly suggestive of the presence of secondary flow of Prandtl's second kind which is driven by anisotropic Reynolds stresses. Xu & Pollard (2001) showed from their LES calculation that the secondary flow is directed towards the corner along the corner bisector (plane of symmetry) in the case of an internal corner, whereas for the external corner, flow is directed away from the corner along the corner bisector and then flows back towards the wall.

## 4.2. *Secondary flow at early stations*

Streamwise stations, $x = 0.54$ m and 1.07 m, were chosen for extensive measurements with the intention to create a data-base for the computational framework. Mean normal ($V$) and spanwise ($W$) velocity components were measured with a cross-wire at six spanwise stations on both the horizontal and vertical surfaces (see figure 4*a*) at the early streamwise station, $x = 0.54$ m. These spanwise stations were chosen as Pitot static tube measurements were also carried out at these stations, which enabled the
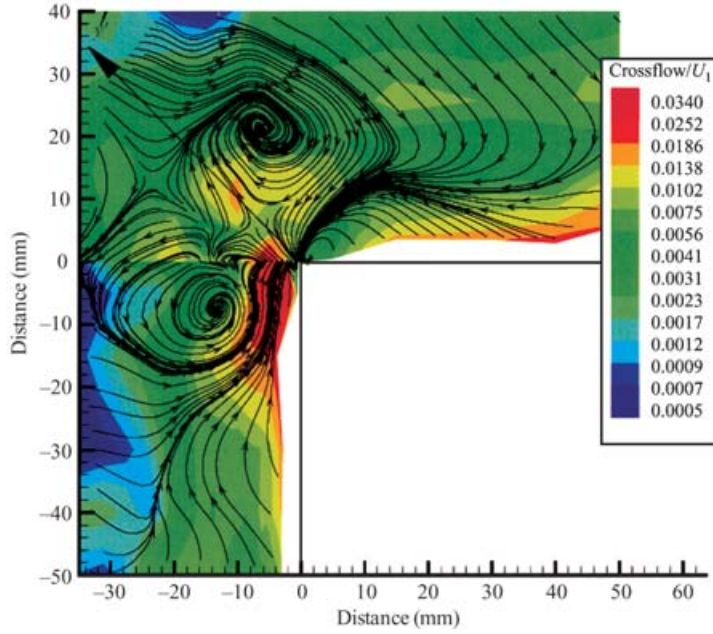
FIGURE 5. Turbulence-driven secondary flow streamlines at $x = 0.54$ m.
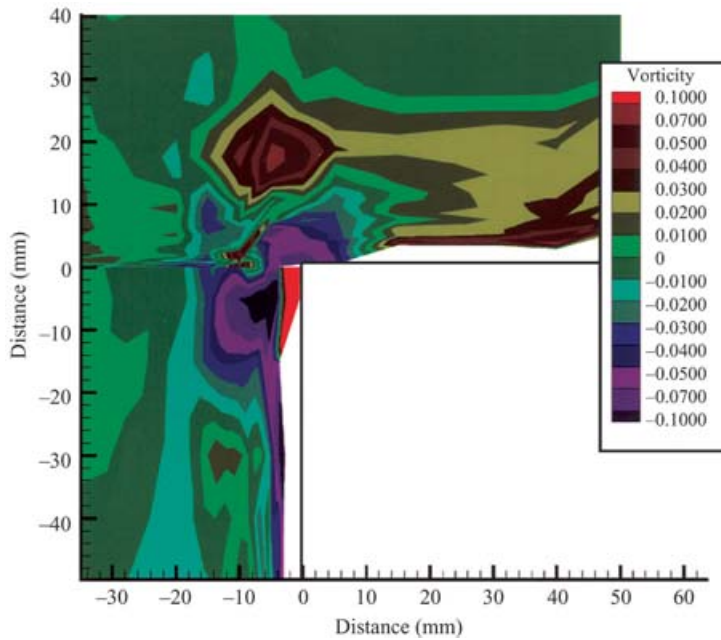


FIGURE 6. Streamwise vorticity distribution at $x = 0.54$ m.

calculation of the friction velocity $U_\tau$. In the corner region measurements were taken at seven stations outward from the corner as shown in figure 4($a$). Secondary flow velocity vectors were plotted and sectional streamlines were drawn by integrating the vector field. Throughout the study, streamlines were drawn using the software 'Tecplot'
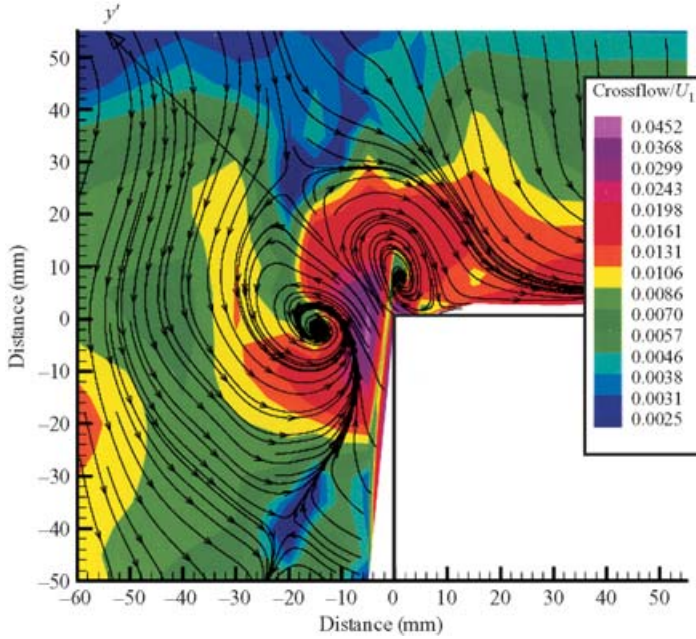
FIGURE 7. Turbulence-driven secondary flow streamlines at $x = 1.07$ m.
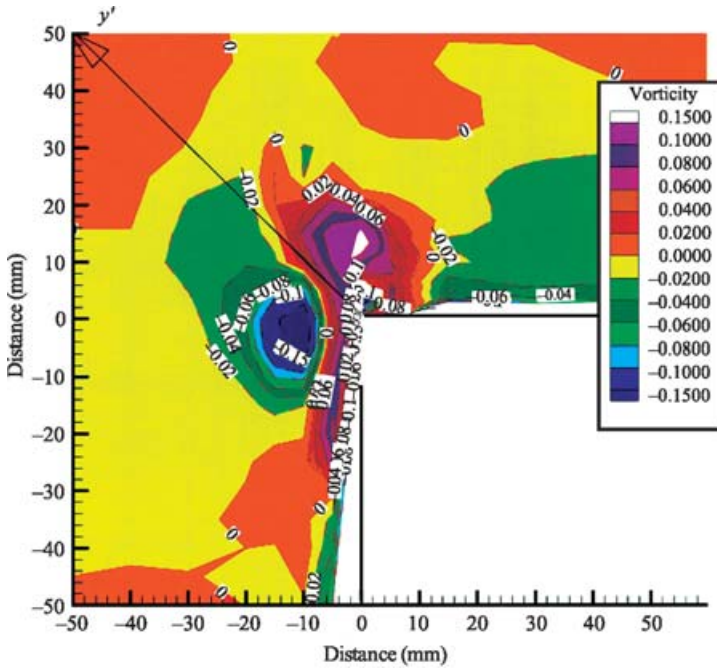


FIGURE 8. Streamwise vorticity distribution at $x = 1.07$ m. Dashed contour lines illustrates negative vorticity.

which uses a two-step, second-order Runge–Kutta method to calculate streamlines. By taking the derivatives of $V$ and $W$, longitudinal vorticity was calculated. Sectional streamlines and secondary flow vorticity distribution at $x = 0.54$ m, are plotted in

figures 5 and 6 respectively. Although it was expected that one pair of counter-rotating vortices would be found, surprisingly two pairs of such vortices were found. The larger pair (located further away from the corner) is the dominant one, whereas the smaller and weaker pair (located very close to the corner) may be attributed to irregularities caused by the screen of the tunnel as mentioned by Perkins (1970). It was expected that on moving downstream the smaller pair of vortices would either dissipate or merge with the larger one. At this streamwise station it is observed that along the corner bisector (in the $y'$-direction) up to 10 mm from the corner the secondary flow is directed towards the corner. A saddle point is located at approximately 10 mm and a second saddle point is located at approximately 20 mm outward from the corner along the corner bisector. Beyond the first saddle point the secondary flow is directed away along the corner bisector. The large vortices are not quite symmetrically placed about the corner bisector. In figure 5, the contours of the secondary (cross) flow magnitude, i.e. $(V^2 + W^2)^{0.5}$, are also shown. Values for the contour levels are given at the right side of the figure. Maximum secondary velocity is found to be 3.4% of the local free-stream velocity, which is found near the corner as well as very close to the surfaces. In figure 6, vorticity is non-dimensionalized by multiplying by $\delta_{2D}/U_1$. At the location of the clockwise vortices, the vorticity is positive and it is negative where the vortices rotate anticlockwise. This phenomenon was explained by Gessner (1973) using the following relationship:

$$\Gamma = \int_A \Omega_x \, \mathrm{d}A = \oint_C U_s \, \mathrm{d}r. \tag{4.1}$$

Here $\Gamma$, $\Omega_x$ and $U_s$ represent circulation, streamwise vorticity and secondary velocity respectively along the sectional streamline; $\mathrm{d}r$ is a differential position vector along $C$, a simple closed curve in the transverse plane ($y, z$ or $s, n$) and $A$ is the area bounded by that curve. On the basis of equation (4.1), a positive value of $\Omega_x$ indicates clockwise vorticity. Maximum vorticity is found to be $\pm 0.10$ approximately at the centre of the vortices.

To measure mean normal ($V$) and spanwise ($W$) velocity components at $x = 1.07$ m, cross-wire measurements were taken at the locations as shown in figure 4(b). Sectional streamlines and secondary flow vorticity distribution are plotted in figures 7 and 8 respectively. As predicted, at this station only one pair of counter-rotating vortices was found. The vortices are almost symmetrically placed around the corner bisector. It is also observed that the secondary flow is completely directed away from the corner bisector and then returned to the wall. A prominent saddle point is located approximately $y' = 25$ mm outward from the corner along the corner bisector. Another is located in the horizontal region (at $s = 8$ mm and $n = 2$ mm) and a third in the vertical region (at $s = 40$ mm and $n = 20$ mm). The secondary flow returns to the wall at approximately $s = 21$ mm, i.e. at $0.65 \, \delta_{2D}$ away from the corner. Maximum secondary velocity is found to be 4.6% of the local free-stream velocity and is observed close to the corner. The vorticity field (non-dimensionalized by multiplying by $\delta_{2D}/U_1$) is shown in figure 10. Positive vorticity is observed near the horizontal surface, whereas negative vorticity is found near the vertical surface. At the centre of the vortices, maximum vorticity is found to be $\pm 0.15$.

### 4.3. Secondary flow at a downstream station

Figure 9 shows the cross-wire measurement points at a downstream station ($x = 4.565$ m). Sectional streamlines and secondary flow vorticity distribution at
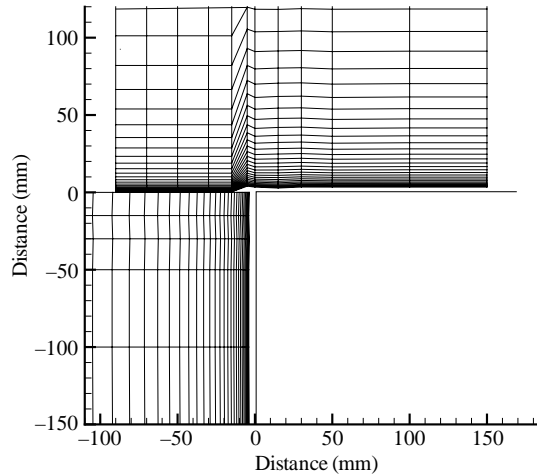
FIGURE 9. Cross-wire measurement grid at $x = 4.565$ m.

$x = 4.565$ m, are plotted in figures 10 and 11 respectively. At this station one pair of counter-rotating vortices is found and the vortices are almost symmetrically placed around the corner bisector. These findings suggest that in an ideal situation only one pair of counter-rotating helical streamwise vortices is symmetrically placed around the corner bisector. The phenomenon of secondary flow directing away from the corner bisector and then returning to the wall is also observed here. Three saddle points are located at this streamwise location, one each in the corner region, vertical region and horizontal region. The first saddle point (in the corner region) is located approximately 70 mm outward from the corner along the corner bisector. Over the vertical surface, another saddle point is quite displaced from the surface and located at $s = 125$ mm and $n = 65$ mm. Over the horizontal surface a further saddle point, which is difficult to identify, is located at $s = 22$ mm and $n = 2$ mm. The secondary flow is observed to return to the wall at $s = 50$ mm at this station which is $0.7\delta_{2D}$ away from the corner. This value is very similar to the case at $x = 1.07$ m. Maximum secondary velocity is again found to be 4.6% of the local free-stream velocity and is observed just near the corner (see figure 10). In figure 11, the secondary flow vorticity distribution is plotted. Positive vorticity is observed near the horizontal surface (where clockwise vortices are located), whereas negative vorticity is found near the vertical surface (where anticlockwise vortices are located). Maximum vorticity is $\pm 0.15$ located at the centre of the vortices.

## 5. Reynolds normal stresses

As the measurements were expected to have much better spatial resolution at the downstream station, i.e. $x = 4.565$ m, in this section data from this station are discussed first and emphasis is given to their analysis. Moreover at this station, beside cross-wire measurements, single-wire measurements were also taken which enabled us to measure streamwise turbulence intensity very close to the surfaces. At the upstream stations, only cross-wire measurements were taken.
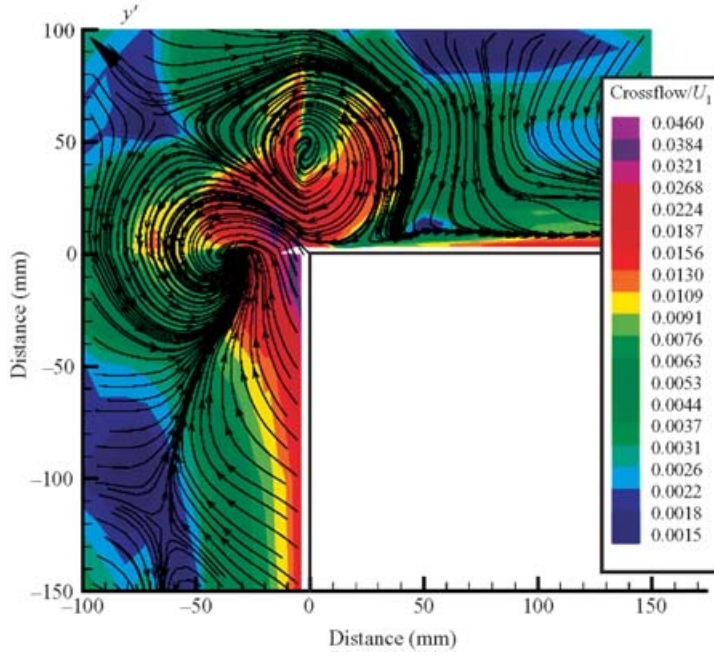
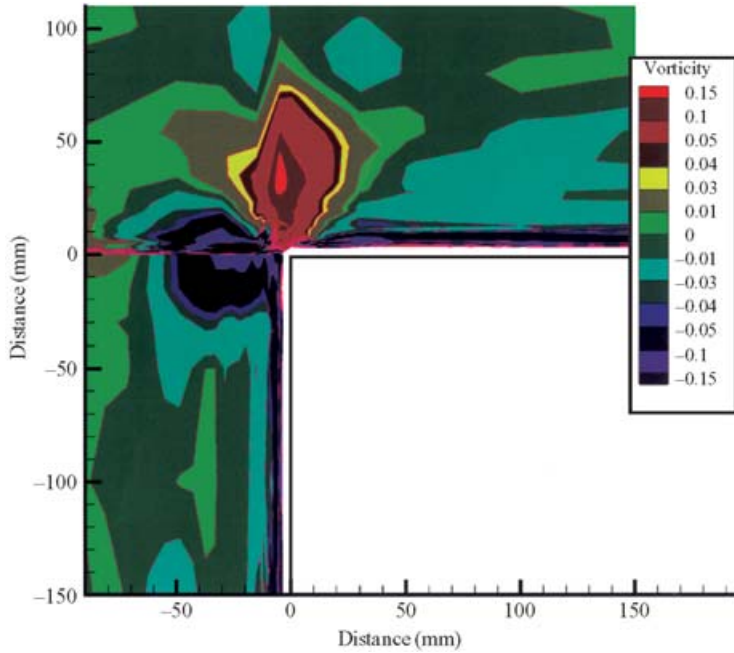FIGURE 10. Turbulence-driven secondary flow streamlines at $x = 4.556$ m.



FIGURE 11. Streamwise vorticity distribution at $x = 4.556$ m. Dashed contour lines illustrates negative vorticity.
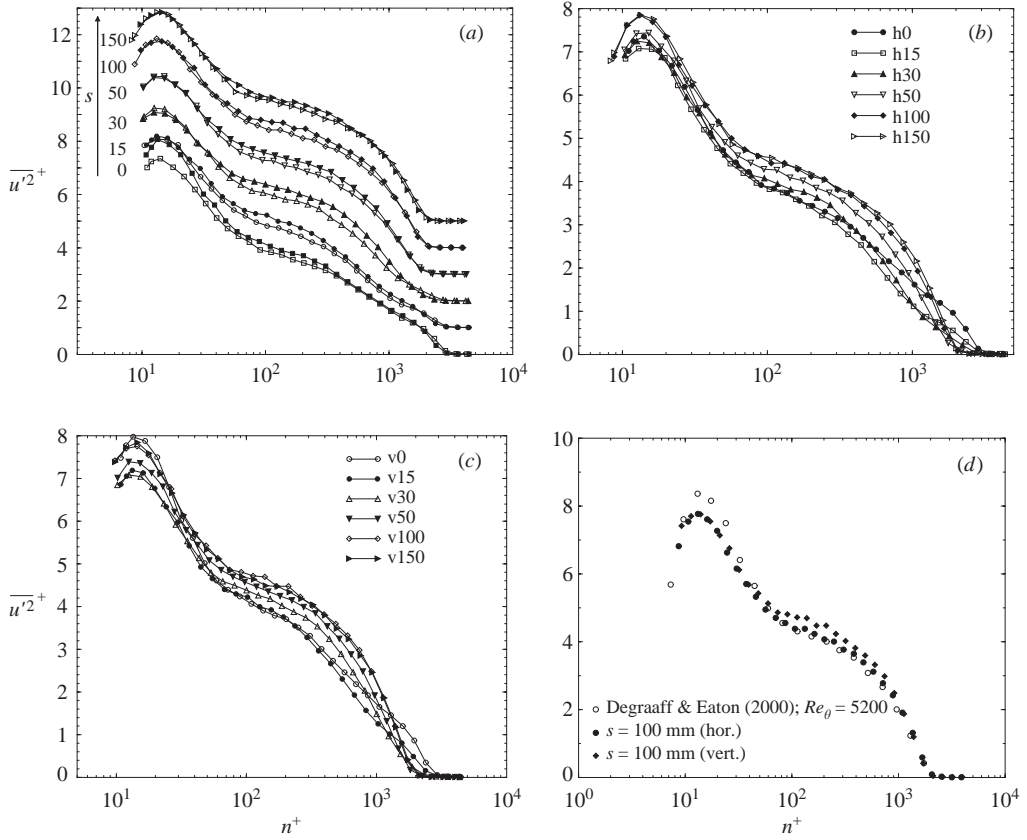
FIGURE 12. (*a*) Comparison of streamwise turbulence intensity profiles at equal spanwise distance from the corner. Open symbols horizontal, filled symbols vertical. (*b, c*) Composite graph for all streamwise turbulence intensity profiles on the horizontal and vertical surface respectively at $x = 4.565$ m. (*d*) Comparison of two-dimensional streamwise turbulence intensity profiles with Degraaff & Eaton (2000). Data, presented in this figure, also appeared in Moinuddin *et al.* (2002*b*).

## 5.1. *Measurements at the downstream station*

### 5.1.1. *Streamwise turbulence intensity*

The streamwise turbulence intensity profiles were measured with a single hot-wire at $x = 4.565$ m. Details of the single-wire data are presented in Moinuddin *et al.* (2002*b*). In this paper only the salient features are touched upon. Six spanwise profiles were obtained on both surfaces at locations shown in figure 9 (same location as the cross-wire profiles). Streamwise Reynolds normal stresses ($\overline{u'^2}^{+}$) are plotted in inner flow scaling (logarithmic) in figure 12(*a*). Here $\overline{u'^2}^{+}$ is the non-dimensional form of streamwise primary Reynolds normal stresses normalized by the square of the local friction velocity i.e. $\overline{u'^2}/U_\tau^{2}$. Spanwise distances of the profiles, in mm from the corner are given in the figure. It is observed that just on the corner, the profile on the horizontal surface has a higher peak than the profile on the vertical surface. Both profiles collapse fairly well in the inertial sublayer and beyond ($n^{+} > 30$). Profiles further away from the corner exhibit more similarity and agreement. This finding is different from that of Panchapakesan & Joubert (1999) who found that both the

mean streamwise velocity profiles and streamwise turbulence intensity profiles do not show similarity on the horizontal and vertical surfaces which may be attributed to the sidewall contamination (for details see Moinuddin *et al.* 2003).

Composite graphs for all the profiles of $\overline{u'^2}^+$ on the horizontal and vertical surfaces are shown in figures 12(*b*) and 12(*c*) respectively. In both the figures it can be seen that the peak values of all the intensity profiles occur at approximately $n^+ = 14$. This is in excellent agreement with the findings of Degraaff & Eaton (2000) and Sreenivasan (1988). Another important feature of these figures is the thicknesses of the intensity layers. The term 'intensity layer' is used here to represent the distance away from the surface where turbulence intensity becomes negligible. The corner has profound effects on the turbulence intensity distribution. Profiles near the corner have an extended intensity layer. The intensity layer gradually thins on moving away from the corner, to $s = 50$ mm and from there it starts thickening to an asymptotic level. The peak values of the intensity profiles behave in a similar way to the thickness of the intensity layer. Very high peaks are observed at the corner in both figures 12(*b*) and 12(*c*). The peak values of the intensity profile decrease gradually as one moves further from the corner (up to $s = 15$ mm in figure 12*b* and $s = 30$ mm in figure 12*c*) and from there the peak values increase to an asymptotic level at $s = 100$ mm. Xu & Pollard (2001) only reported a decrease of peak values further from the corner. In fact they normalized their data with averaged $U_\tau$ instead of local $U_\tau$. Moinuddin *et al.* (2003) reported that local $U_\tau$ near the corner is quite high and it decays exponentially towards the two-dimensional region. Had their profiles been normalized by local $U_\tau$, they might have shown similar peak value patterns to the current study.

### 5.1.2. *Comparison of two-dimensional streamwise turbulence profile*

Based on the findings that at $s = 100$ mm, a ZPG nominal two-dimensional boundary layer exists, the turbulence intensity profiles on both surfaces are compared with that of Degraaff & Eaton (2000) at $Re_\theta$ 5200 as shown in figure 12(*d*). The profiles agree fairly well in the inertial sublayer and beyond ($n^+ > 70$). A large difference of intensity is observed in the viscous sublayer and buffer region ($n^+ < 20$). In fact intensity values very close to the wall including the peak value are still subject to debate. Different researchers have found different values. Mochizuki & Nieuwstadt (1996) based on a survey of many independent experimental and numerical studies for ZPG boundary layer flow, found that $(u'^+)_{max}$ has a weak dependence on $Re_\theta$. The relationship is

$$(u'^+)_{max} = 0.000015(Re_\theta) + 2.67. \tag{5.1}$$

According to this relationship $(u'^+)_{max}$ based on $Re_\theta$ 5700 should be 2.7555 which is within 1% of our $(u'^+)_{max}$ value of 2.785. Mochizuki & Nieuwstadt (1996) also suggested that $(u'^+)_{max}$ can be considered independent of $Re_\theta$ and $(u'^+)_{max}$ should fall within the range of 2.71 ±0.14. Our $(u'^+)_{max}$ value of 2.785 also falls in that range.

### 5.1.3. *Secondary Reynolds normal stresses*

With the cross-wire, turbulence intensity in the *x*-, *n*- and *s*-directions was measured. Reynolds normal stresses are denoted as $\overline{u'^2}^+$, $\overline{v'^2}^+$ and $\overline{w'^2}^+$ respectively; $\overline{v'^2}^+$ and $\overline{w'^2}^+$ are the non-dimensional form of secondary Reynolds normal stresses in the normal and spanwise directions, normalized by the square of the local friction velocity ($U_\tau^2$). Cross-wire measurements were carried out at the same stations as where single-wire measurements were taken. The streamwise turbulence intensity profiles measured with both a single wire and cross-wires collapse quite well. Furthermore, as it was found
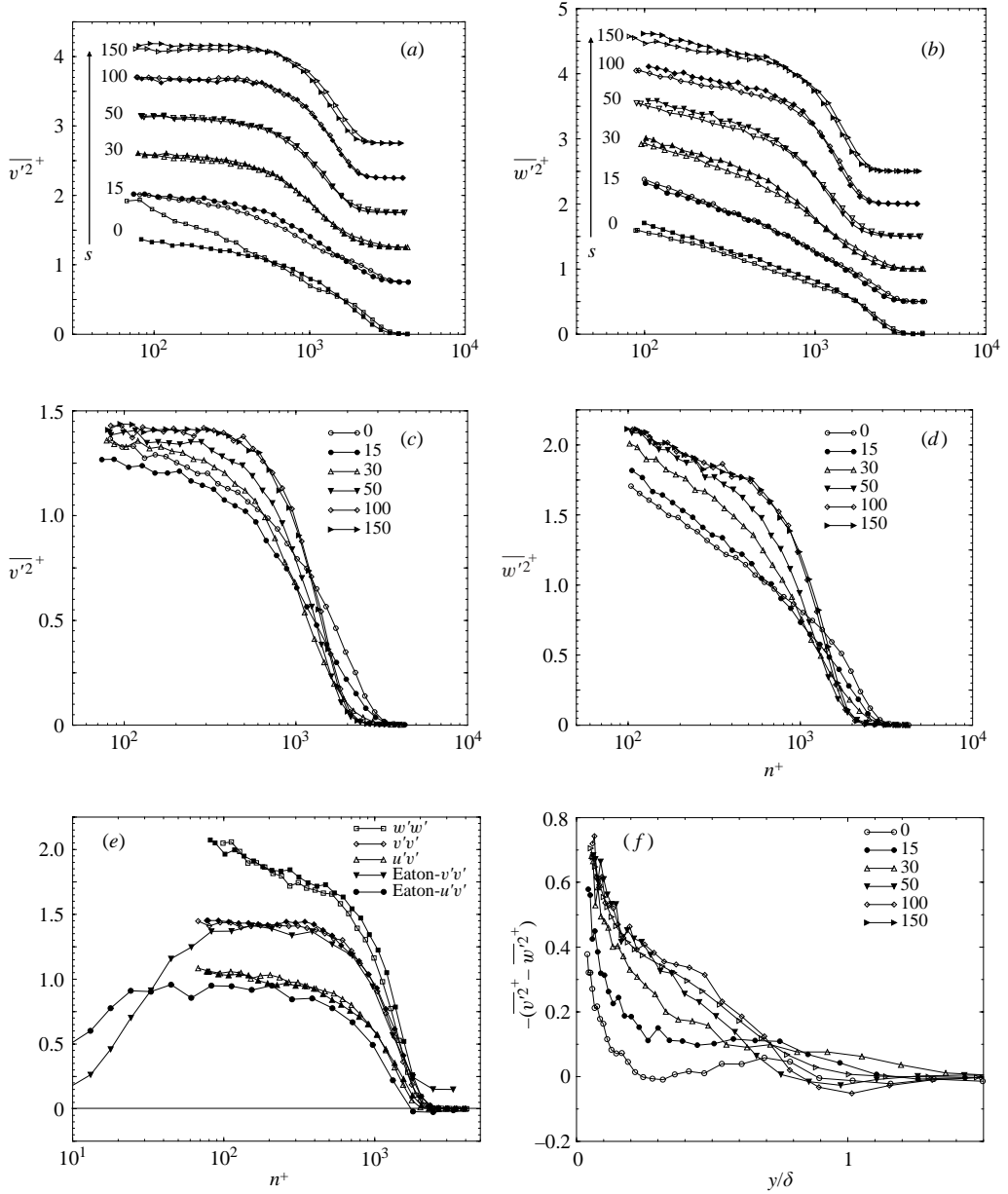
FIGURE 13. $(a,b)$ Comparison of $(\overline{v'^2}^+)$ and $(\overline{w'^2}^+)$ profiles at equal spanwise distance from the corner. Open symbols horizontal, filled symbols vertical; in $(a)$ $s = 15$ shifted 0.75 and the rest 0.5 units up, in $(b)$ all shifted 0.5 units up $(c,d)$ composite graph for all $\overline{v'^2}^+$ and $\overline{w'^2}^+$ profiles on the vertical surface respectively at $x = 4.565$ m. $(e)$ Comparison of two-dimensional secondary normal stress and primary shear stress profiles with Degraaff & Eaton (2000)'s LDV data. $(f)$ Separation of the secondary normal stresses.

that a ZPG nominal two-dimensional boundary layer exists at $s = 100$ mm, the $\overline{v'^2}^+$ and $\overline{u'v'}^+$ profiles on both surfaces are compared with that of Degraaff & Eaton (2000) at $Re_\theta = 5200$ as shown in figure 13($e$). The profiles agree fairly well. Profiles
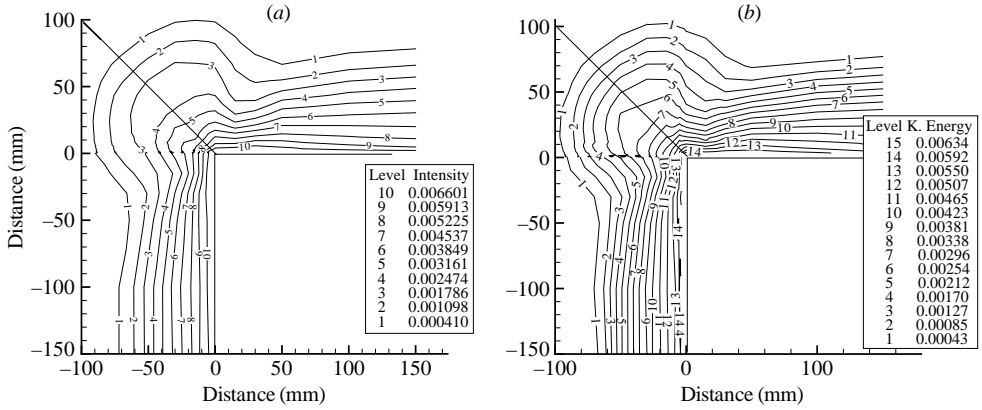
FIGURE 14. (a) Streamwise isointensity ($\overline{u'^2}/U_1^2$) contour plots, after Moinuddin *et al.* (2002*b*). (b) Contour plots of kinetic energy ($0.5(\overline{u'^2} + \overline{v'^2} + \overline{w'^2})/U_1^2$) distribution.

of $\overline{w'^2}^+$ could not be compared as it was not presented by Degraaff & Eaton (2000); however these profiles on both the surfaces show (figure 13*e*) very good similarity.

Profiles of $\overline{v'^2}^+$ and $\overline{w'^2}^+$ are plotted with inner flow scaling (logarithmic) in figures 13(*a*) and 13(*b*) respectively. Spanwise distances of the profiles, in mm from the corner, are given in the figure. For $\overline{v'^2}^+$, higher values are observed in the inertial sublayer region ($n^+ < 400$) at the corner for the horizontal surface than for the vertical surface; however both the profiles collapse in the outer region. Profiles of $\overline{v'^2}^+$, at the same spanwise stations, further away from the corner exhibit more similarity and agreement compared to the corner profiles. The same phenomenon was observed for the $\overline{u'^2}^+$ profiles. A different phenomenon was observed for $\overline{w'^2}^+$, where profiles exhibit similarity right from the corner.

In figures 13(*c*) and 13(*d*) composite graphs for all the $\overline{v'^2}^+$ and $\overline{w'^2}^+$ profiles on the vertical surface are presented. Like the $\overline{u'^2}^+$ profiles, for both the $\overline{v'^2}^+$ and $\overline{w'^2}^+$ profiles, the corner effect on the thickness of the intensity layer is clearly observed. Profiles near the corner have an extended intensity layer. Moving further away from the corner it gradually thins and then starts thickening to an asymptotic level. Higher stress components are found near the corner and they behave in a similar way to the thickness of the intensity layer. An initial decreasing and then increasing of the secondary stress magnitude from the corner towards the two-dimensional region was observed, which is similar to the case of primary normal stress.

In figure 13(*f*) an important parameter ($\overline{w'^2}^+ - \overline{v'^2}^+$) is plotted with outer flow scaling (linear). Demuren & Rodi (1984), Perkins (1970) and many other researchers indicated that the gradient of ($\overline{w'^2}^+ - \overline{v'^2}^+$) is one of the major driving forces of the secondary motion. Demuren & Rodi (1984) termed it the separation of the secondary normal stresses. From the figure 13(*f*) it is clearly seen that near the corner, the gradient is much steeper than those away from the corner. Thus near the corner, the magnitude of the secondary flow is quite large, which is consistent with figure 10.

### 5.1.4. *Isointensity contours*

The isointensity contours plots are presented in figure 14. Commensurate with the intensity profiles on both surfaces, measurements of Reynold stresses were also taken with both single and cross-wires at seven spanwise stations in the corner region; $\overline{u'^2}$

is normalized by the square of the local free-stream velocity ($U_1^2$) and streamwise isointensity contours are plotted in figure 14(*a*). The edge of the intensity layer (where $\overline{u'^2}/U_1^2 = 4.10255 \times 10^{-4}$) grows almost equally about the plane of symmetry. A depression of the contours can be observed along the plane of symmetry. This depression is absent in the data of Xu & Pollard (2001). Kinetic energy, $k$, is calculated as $k = 0.5(\overline{u'^2} + \overline{v'^2} + \overline{w'^2})$ and is also normalized by $U_1^2$. Contour plots of kinetic energy distribution are shown in figure 14(*b*) and a depression of the contours along the corner bisector is again obvious. Along the plane of symmetry, secondary flow is directed away from the corner and then returns back towards the wall further from the corner. From the corner to the returning point, the presence of a considerable cross-flow component attenuates the turbulence intensity, "... because the circulatory nature of secondary flow would normally be expected to depress stress levels along a corner bisector..." (Gessner, Po & Emery 1979). In line with their explanation it can be stated that as the fluid is convected outwards along the corner bisector, the fluid retains some of its statistical properties. Similar to the boundary layer, the initial thinning and then thickening of both the streamwise intensity layer and kinetic energy layers can be seen as one moves from the two-dimensional region towards the corner.

The data of Xu & Pollard (2001) show strong interaction between the secondary flows developed on internal and external corners. This is evidenced by the fact that at the centre of the co-axial square duct the turbulence intensity never goes to zero. At the wall bisector their outer wall is located approximately 3.5 boundary layer thicknesses from the inner wall. In the present study the outer wall is located 9 boundary layer thicknesses (at $x = 4.565$ m) from the chine. Moreover the slotted tunnel wall reduces the growth of the boundary layer on the outer (tunnel) wall. It is, therefore, expected that the boundary layer on the chine is free from the interference of the outer wall.

### 5.2. *Measurements at early stations*

At these early stations $x = 0.54$ m and $1.07$ m, no single-wire measurements were taken. Turbulence intensities in all three cardinal directions were measured with the cross-wires. Spanwise stations where cross-wire measurements were carried out are shown in figure 4. Due to space constraints only the data at $x = 0.54$ m are presented in the current paper. Furthermore data at $x = 1.07$ m are almost similar to those for $x = 0.54$ m. Data at $x = 1.07$ m will be found in Moinuddin (2003). The Reynolds normal stress profiles ($\overline{u'^2}^+$, $\overline{v'^2}^+$ and $\overline{w'^2}^+$) are plotted at equal spanwise distances from the corner in figure 15. All the profiles are plotted with inner flow scaling (logarithmic) and spanwise distances of the profiles, in mm from the corner, are given in the figure. For all three normal stresses, strong asymmetry of the profiles is observed up to $s = 15$ mm, mainly in the inertial sublayer (up to $n^+ \approx 300$). At $x = 1.07$ m, strong asymmetry is only observed near the corner. Reynolds stress profiles, beyond $s = 15$ mm on both surfaces, agree fairly well.

Moinuddin *et al.* (2003) reported that further from the corner, the flow develops as a ZPG nominal two-dimensional boundary layer flow. Therefore, at $x = 0.54$ m, the $\overline{v'^2}^+$ and $\overline{w'^2}^+$ profiles at $s = 40$ mm on both the surfaces are compared with that of Erm (1988) at $Re_\theta = 1600$ as shown in figure 15(*d*). In both cases the profiles are in excellent agreement. Similarly at $x = 1.07$ m the $\overline{v'^2}^+$ and $\overline{w'^2}^+$ profiles are also found to be in very good agreement with that of Erm (1988) at $Re_\theta = 2780$.

Composite graphs for all three normal stress and primary shear stress profiles on the horizontal surface are presented in figure 16. Unlike the downstream station, at both the upstream stations ($x = 0.54$ m and $1.07$ m), for all three Reynolds stress
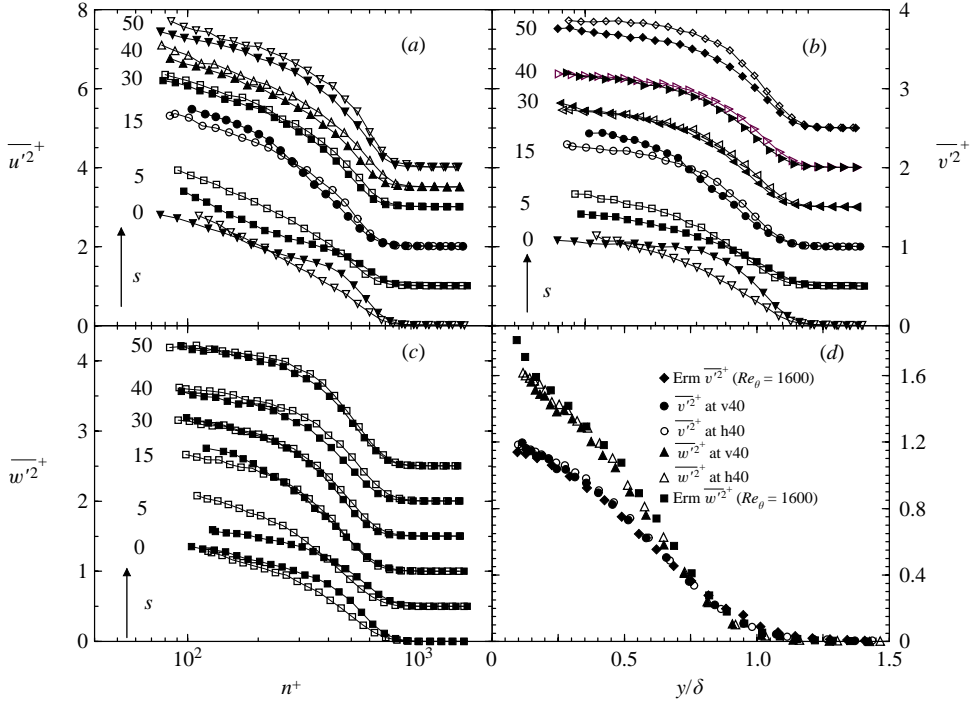
FIGURE 15. Turbulence intensity profiles at $x = 0.54$ m. Comparisons of Reynolds normal stress profiles $(\overline{u'^2}^+, \overline{v'^2}^+$ and $\overline{w'^2}^+)$ at equal spanwise distance from the corner shown in $(a)$, $(b)$ and $(c)$ respectively. Open symbols horizontal, filled vertical. $(d)$ Comparison of two-dimensional secondary normal stress profiles with Erm's (1988) data.
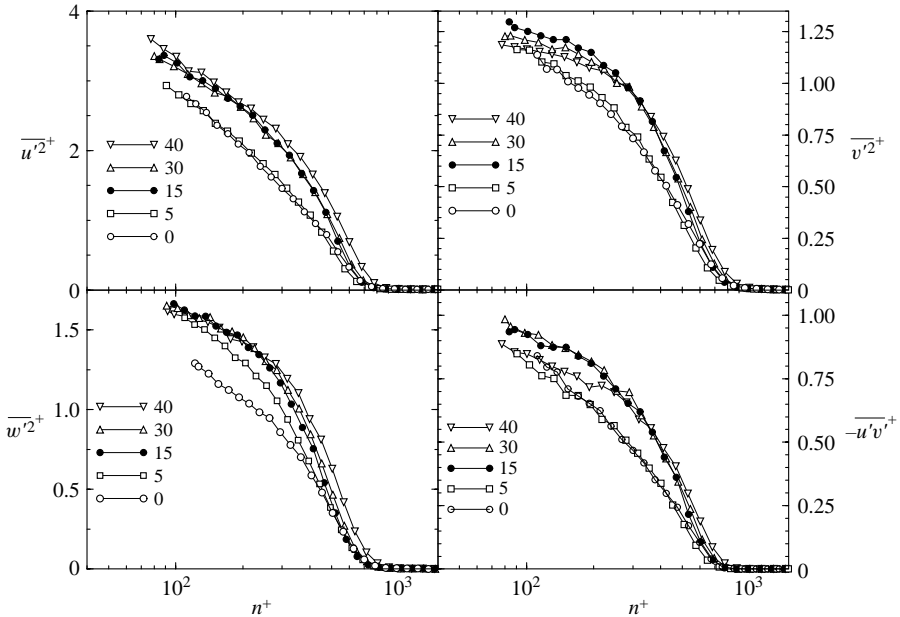


FIGURE 16. Composite graph for all Reynolds normal stress profiles, to show corner effect on stress profile, over the horizontal surface at $x = 0.54$ m.
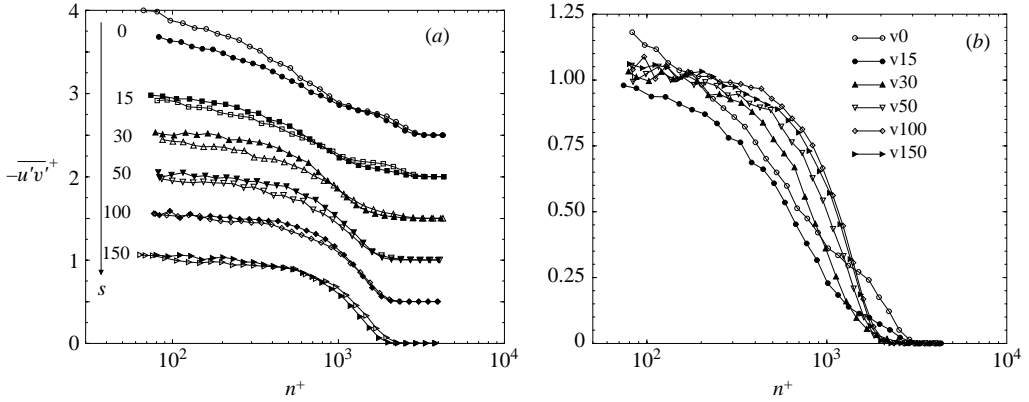
FIGURE 17. (*a*) Comparison of Reynolds shear stress (in $x, n$ plane) profiles at equal spanwise distance from the corner. Open symbols horizontal, filled vertical. (*b*) Composite graph for all profiles on the vertical surface at $x = 4.565$ m.

($\overline{u'^2}^+$, $\overline{v'^2}^+$ and $\overline{w'^2}^+$) profiles, very little corner effect on the thickness of the intensity layer is observed. Profiles at different spanwise stations have almost the same intensity layer thickness. Again unlike the downstream station, at $x = 0.54$ m, lower stress components are found near the corner for all three normal stresses. Moving further from the corner towards the two-dimensional region the magnitude of $\overline{u'^2}^+$ and $\overline{w'^2}^+$ gradually increases to an asymptotic level. In contrast, $\overline{v'^2}^+$ gradually increases up to $s = 15$ mm in the inertial sublayer and then decreases up to the two-dimensional region while moving away from the corner. The same phenomenon is also observed for the primary shear stress ($\overline{-u'v'}^+$) profiles. However, at $x = 1.07$ m higher stress magnitude for all three Reynolds normal stress ($\overline{u'^2}^+$, $\overline{v'^2}^+$ and $\overline{w'^2}^+$) profiles are found near the corner and they behave in a similar way to those downstream rather than those at the upstream station. Moving further from the corner towards the two-dimensional region, initial decreasing of the magnitude of the secondary stress is observed up to $s = 5$ mm and then an increase to an asymptotic level.

## 6. Reynolds shear stresses

### 6.1. *Primary shear stresses*

Primary shear stress is another important parameter, which Gessner (1973) suggests is responsible for generating the secondary flow. Due to space constraints, this parameter is discussed only for the downstream station ($x = 4.565$ m), where the spatial resolution is better. Profiles of $\overline{u'v'}^+$ (normalized by $U_\tau^2$) at the same spanwise distance on both the surfaces are plotted in figure 17(*a*). It has been observed that like the normal stresses, just on the corner, the shear stress profile on the horizontal surface has a higher level of stress than the profile on the vertical surface. Profiles further away from the corner exhibit more similarity and agreement. In figure 17(*b*) a composite graph for all the $\overline{u'v'}^+$ profiles on the horizontal surface is plotted. The effects of the corner on the thickness of the stress layer and magnitude of the stress level is also seen here. Profiles near the corner have an extended intensity layer. Moving further away from the corner, its thickness gradually reduces up to $s = 50$ mm and from there onwards gradually expands to an asymptotic level. The initial decreasing and then increasing of the magnitude of the secondary stress from the corner towards the two-dimensional region is also evident.
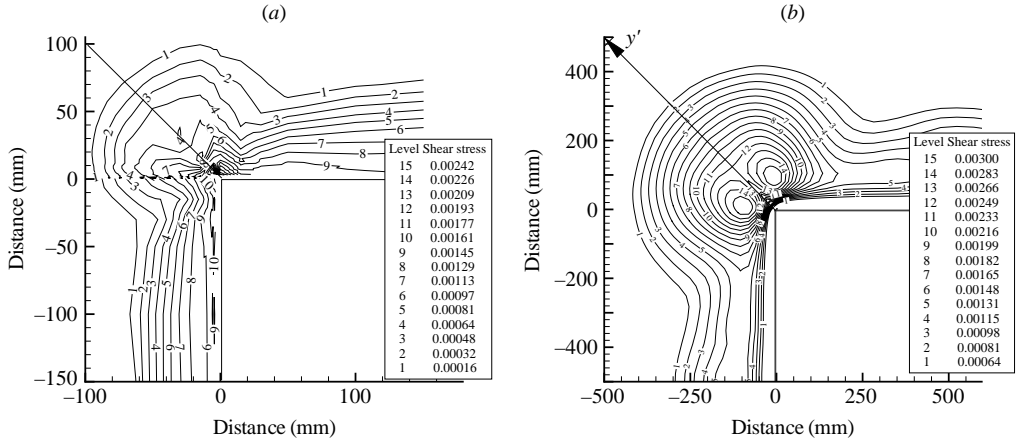
FIGURE 18. Contour plots of the resultant primary shear stress. (*a*) From the current study at
$x = 4.565$ m and (*b*) drawn using Xu & Pollard's (2001) data.

The distribution of the resultant primary shear stress $(\overline{u'v'}^2 + \overline{u'w'}^2)^{0.5}/U_1^2$ is shown in figure 18(*a*). The primary shear stress levels grow almost equally about the plane of symmetry. In this contour plot a deep depression along the plane of symmetry is observed. This phenomenon is consistent with the arguments of Gessner *et al.* (1979) (as mentioned in §5.1.4). Data from Xu & Pollard (2001) are plotted in figure 18(*b*). There is a clear difference in spatial distribution between the current study and their study.

### 6.2. *Secondary shear stress*

Secondary shear stress $\overline{v'w'}$ is another statistical quantity which may contribute to secondary flow. Unfortunately this quantity is very difficult to measure and Bradshaw (1987) stated that there was no reliable experimental technique available to measure $\overline{v'w'}$ accurately. Even to date no such appropriate technique has been developed. The measurements of this statistical quantity in the internal corner region by two separate groups, Brundrett & Baines (1964) and Gessner and co-workers, have been ignored by turbulence modellers when validating their codes. Demuren & Rodi (1984) summarized Perkins's (1970) argument of the two different contributing mechanisms for the generation of $\overline{v'w'}$. The first mechanism is associated with the gradients of the secondary velocities, and their contribution to $\overline{v'w'}$ can be represented in terms of an isotropic eddy viscosity. The second mechanism is associated with the distortion of the primary stress field in the corner and is therefore associated with the primary velocity gradients. Perkins (1970) expected that the contribution of both mechanisms are of equal magnitude. Demuren & Rodi (1984) stressed the importance of representing both processes in a mathematical model.

## 7. Origin of turbulence-driven secondary flow

Prandtl (1926) was the first to suggest that the secondary motion of the second kind is caused by the turbulence field. A rigorous analysis by Einstein & Li (1958) showed that the non-uniform gradient of the Reynolds stresses gives rise to the secondary motion. To identify the contributions from shear and normal stresses, Bradshaw (1987) used the mean streamwise vorticity equation (1.1) for statistically stationary flows. As mentioned early in the paper, the contribution to the production or destruction of streamwise vorticity from Reynolds secondary shear stresses and normal stresses is represented by terms (A4) and (A5) of equation (1.1) respectively.
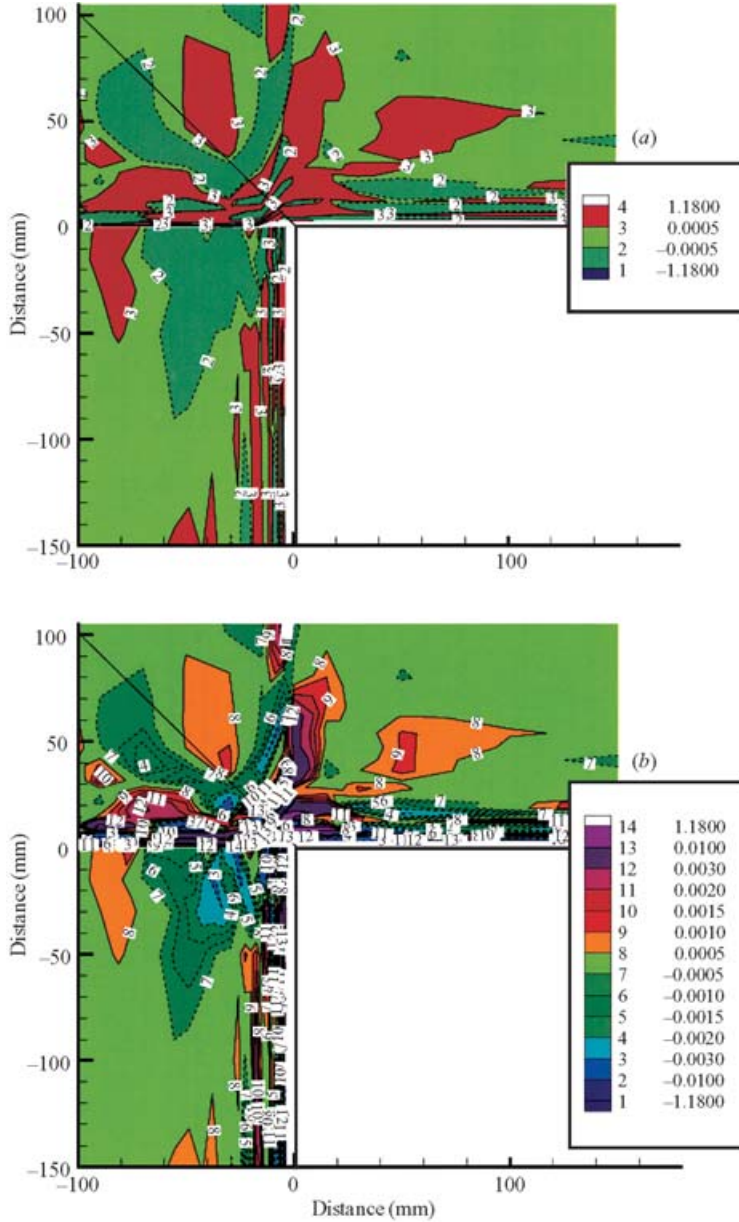
FIGURE 19. Distribution of the mean streamwise vorticity production by normal stress contribution at $x = 4.565$ m: (a) only the regions of positive and negative production, and (b) detailed contours of the vorticity production.

Xu & Pollard (2001) reported that turbulent secondary flow generation around the internal corner presents a different spatial distribution to that of an external corner in the co-axial square duct. They found that in the vicinity of the external corner the contribution from the secondary shear stress (A4) is dominant. In Xu & Pollard (2001) a butterfly-shaped structure with alternate positive and negative contributing regions was shown for both secondary shear and normal stresses. From the present study regions of positive and negative mean streamwise vorticity production by normal stresses, (A5), normalized by multiplying by $\delta_{2D}^2/U_1^2$, are plotted in figure 19(a).

Though the graph is not exactly butterfly shaped, it resembles a butterfly structure with alternate positive and negative regions. In figure 19(*b*) detailed contours of the mean streamwise vorticity production by normal stress are plotted. The secondary shear stress contribution could not be determined due to the lack of reliable experimental techniques. Work is at present proceeding to calculate this flow numerically. Current experimental results at early stations are being used as boundary conditions. It is expected that secondary shear stress ($\overline{v'w'}$) will be calculated and then it would be possible to find the origin of secondary flow of the second kind.

## 8. Conclusions

Detailed hot-wire measurements in the corner region of a chine are presented for the symmetrical flow over two orthogonal surfaces. The study shows that very near the corner, the maximum values of all the Reynolds stress profiles are higher than the neighbouring profiles and they decrease gradually to a minimum at successive spanwise stations further from the corner and then increase to an asymptotic level in the two-dimensional region. Mean streamwise velocity and all the Reynolds stress profiles near the corner extend to a greater distance away from the surface before reaching the region of free-stream velocity and negligible turbulence intensity respectively. Moving further away from the corner the profiles initially thin and from there inwards they start thickening to an asymptotic level. In the contours of streamwise mean velocity, streamwise turbulence intensity and kinetic energy distribution, the initial thinning and then thickening of the boundary layer, intensity layer and energy layer can be seen as one moves from the two-dimensional region towards the corner.

An important aspect of this work is the experimental observation of a pair of counter-rotating vortices symmetrically placed around the external corner. The secondary flow is found to be directed outward along the corner bisector and then returned back to the surface approximately $0.7\delta_{2D}$ from the corner. The mean secondary flow is found to be driven by anisotropy of the Reynolds stresses but whether secondary shear stress or normal stress dominates could not be determined. As the fluid is convected outwards along the corner bisector it retains some of its statistical properties and the turbulence intensity is attenuated. Consequently a depression of the contours in all turbulence intensity contour plots is observed along the plane of symmetry.

REFERENCES

BRADSHAW, P. 1987 Turbulent secondary flows. *Annu. Rev. Fluid Mech.* **19**, 53–74.

BRUNDRETT, E. & BAINES, W. D. 1964 The production and diffusion of vorticity in duct flow. *J. Fluid Mech.* **19**, 375–394.

DAVIES, E. B. & YOUNG, A. D. 1963 Streamwise edge effects in the turbulent boundary layer on a flat plate of finite aspect ratio. *Aero. Res. Council R & M* 3367.

DEGRAAFF, D. B. & EATON, J. K. 2000 Reynolds-number scaling of the flat plate turbulent boundary layer. *J. Fluid Mech.* **422**, 319–346.

DEMUREN, A. O. & RODI, W. 1984 Calculation of turbulence driven secondary motion in noncircular ducts. *J. Fluid Mech.* **140**, 189–222.

Durst, F. & Zanoun, E. S. 2002 Experimental investigation of near-wall effects on hot-wire measurements. *Exps. Fluids* **33**, 210–218.

Einstein, H. A. & Li, H. 1958 Secondary currents in straight channels. *Trans. Am. Geophys. Union* **39**, 1085–1088.

Elder, J. W. 1960 The flow past a flat plate of finite width. *J. Fluid Mech.* **9**, 133–153.

Erm, L. P. 1988 Low Reynolds-number turbulent boundary layers. PhD thesis, University of Melbourne.

Gessner, F. B. 1973 The origin of secondary flow in turbulent flow in a corner. *J. Fluid Mech.* **58**, 1–25.

Gessner, F. B. & Emery, A. F. 1981 The numerical prediction of developing flow in rectangular ducts. *Trans. ASME* I: *J. Fluids Engng* **103**, 445–455.

Gessner, F. B. & Jones, J. B. 1965 On some aspects of fully-developed turbulent flow in rectangular channels. *J. Fluid Mech.* **23**, 689–713.

Gessner, F. B., Po, J. K. & Emery, A. F. 1979 The measurements of developing turbulent flow in a square duct. In *Turbulent Shear Flows I* (ed. F. Durst *et al.*), pp. 119–136. Springer.

Kelso, R. M. 1991 A study of free shear flows near rigid boundaries. PhD thesis, University of Melbourne.

Mojola, O. O. & Young, A. D. 1972 An experimental investigation of the turbulent boundary layer along a streamwise corner. *AGARD CP* 93, pp. 12.1–12.9.

Mochizuki, S. & Nieuwstadt, F. T. M. 1996 Reynolds-number dependence of the maximum in the streamwise velocity fluctuations in wall turbulence. *Exps. Fluids* **21**, 218–226.

Moinuddin, K. A. M. 2003 Investigations of turbulence-driven secondary motion over a streamwise external corner. PhD thesis, University of Melbourne.

Moinuddin, K. A. M., Hafez, S., Joubert, P. N. & Chong, M. S. 2001 Experimental study of turbulent flow along a streamwise edge (Chine). *14th Australasian Fluid Mechanics Conference, Adelaide*, pp. 231–234.

Moinuddin, K. A. M., Hafez, S., Joubert, P. N. & Chong, M. S. 2002*a* In search of symmetric turbulent flow along a streamwise edge (Chine). *9th Asian Congress of Fluid Mechanics, Isphahan, Iran.*

Moinuddin, K. A. M., Joubert, P. N. & Chong, M. S. 2002*b* Turbulence intensity distribution for flow along a streamwise external corner. *2002 ASME International Congress for Mechanical Engineers, New Orleans, Louisiana.*

Moinuddin, K. A. M., Joubert, P. N., Chong, M. S. & Hafez, S. 2003 Experimental investigation of turbulent boundary layer developing along a streamwise external corner (Chine). *Expl Thermal Fluid Sci.* **27**, 599–609.

Nikuradse, J. 1930 Turbulente Strömung in nicht-kreisformigen Rohren. *Ing. Arch* **1**, 306.

Österlund, J. M. 1999 Experimental studies of turbulent boundary layer flow. PhD thesis, Department of Mechanics, Royal Institute of Technology, Stockholm.

Panchapakesan, N. R. & Joubert, P. N. 1998 Turbulent boundary layer development along a streamwise edge (Chine)- mean flow. *13th Australasian Fluid Mechanics Conference, Monash, 1998*, pp. 373–376.

Panchapakesan, N. R. & Joubert, P. N. 1999 Turbulence measurements in the boundary layer over a streamwise edge (Chine). *Turbulence and Shear flow Phenomena, Santa Barbara, 1999.*

Perkins, H. J. 1970 The formation of streamwise vorticity in turbulent flow. *J. Fluid Mech.* **44**, 721–740.

Perry, A. E. 1982 *Hot-wire Anemometry*. Clarendon.

Prandtl, L. 1926 Uber die ausgebildete turbulenz. *Verh. 2nd Intl Kong. Fur Tech. Mech.*, *Zurich* [English transl. *NACA Tech. Memo.* 435].

Sreenivasan, K. R. 1988 A unified view of the origin and morphology of the turbulent boundary layer structure. In *Turbulence Management and Relaminarization* (ed. H. Liepmann & R. Narashima). Springer.

Xu, H. & Pollard, A. 2001 Large eddy simulation of turbulent flow in a square annular duct. *Phys. Fluid* **13**, 3321–3337.

Zamir, M. & Young, A. D. 1970 Experimental investigation of the boundary layer in a streamwise corner. *Aero. Q.* **2**, 313–339.